Distributed Acoustic Sensing Over Deployed Telecommunication Fiber Networks: Opportunities and Challenges

Élie Awwad, Maria Freire Hermelo, Diane Prato, Pierre Pruvost, Pallab Kumar Choudhury, Yves Jaouën, Renaud Gabet, and Heming Huang

***Abstract*—In this paper, we highlight opportunities and challenges of deploying Rayleigh-based distributed optical fiber sensing, also known as distributed acoustic sensing (DAS), over existing optical telecommunication networks. We review some of the prominent recent advances in this area and we shed light on future directions. First, we briefly review classifications of DAS systems and we focus on the advantages of using a continuous-wave constant-power DAS probe signal for in-band coexistence between DAS and data transmission over the same fiber. Second, we emphasize on the important role of the mechanical coupling between the fiber, its hosting cable and their surrounding environment in the interpretation of the extracted strain information. Third, we show results on the estimation of distributed birefringence information using a polarization-diversity DAS interrogation. Finally, we study the impact of laser phase noise on continuous-wave constant-power DAS interrogation using phase-encoded probing sequences and attempt to mitigate it.**

***Index Terms*—Distributed acoustic sensing, optical fiber sensing, in-band communication and sensing, cable-to-medium coupling, birefringence monitoring, laser phase noise.**

I. Introduction

As human environments and their supporting infrastructures become increasingly dense and interconnected, ensuring their safety, integrity and sustainability has become a major societal concern. The breadth of these environments and their heterogeneity makes their monitoring a technological challenge. The early detection of hazards, accidental failures, or malicious damage affecting critical infrastructures is essential, as such events can have significant consequences for both operators and end users. Today, infrastructure monitoring relies on a wide range of discrete sensors including surveillance cameras, personal devices, magnetometers, radar-based sensors, and handheld inspection equipment, to monitor road traffic [1], detect intrusions, identify anomalies such as road degradation [2], water distribution leaks [3], or even identify the layout of the telecommunication cable itself [4]. While these sensing modalities are effective for localized monitoring, they inherently suffer from limited spatial coverage, and might suffer as well from reduced sensitivity and non-negligible susceptibility to electromagnetic interference. Furthermore, extending their deployment over large-scale infrastructures is often impractical due to the associated installation, operational and maintenance costs. In contrast, telecommunication optical fiber networks already span cities and interconnect urban and rural areas over thousands of kilometers, making them an attractive sensing infrastructure whose reuse could enable continuous wide-area monitoring without requiring the deployment of additional sensors.

Several distributed optical fiber sensing (DOFS) technologies have been developed, each relying on a different light-scattering mechanism. Raman-based sensing is primarily dedicated to distributed temperature measurements, whereas Brillouin-based techniques provide absolute temperature and strain measurements along the fiber, albeit with limited mechanical bandwidth and vibration sensitivity. Rayleigh-based sensing, commonly known as distributed acoustic sensing (DAS), instead measures relative variations of the optical phase using a highly coherent laser source. Although it does not directly provide absolute physical quantities, DAS offers significantly higher sensitivity and broader mechanical bandwidth, making it particularly well suited for vibration monitoring over existing telecommunication fiber infrastructures [1], [5]–[9]. In this paper, we will cover the challenges and opportunities of using DAS systems over telecommunication fiber networks to monitor relative strain variations.

Despite its strong potential, deploying DAS over lit telecommunication networks remains challenging. Conventional DAS systems are fundamentally limited by the weak Rayleigh backscattered signal and laser phase noise. Dealing with the large volume of sensing data that must be acquired and processed is an extra challenge. Additional constraints arise when moving from dedicated sensing fibers to deployed telecommunication infrastructures. On lit fibers, sensing must coexist with communication channels without degrading network performance, while on both lit and dark fibers the sensing system must operate over complex network topologies including point-to-multipoint fiber links encountered in passive optical networks (PON) [10], [11]. Recent demonstrations have highlighted the ability of DAS to monitor road traffic, human activity, and seismic events over deployed networks [1], [7], [9], [12]–[14]. However, these demonstrations generally involve compromises in terms of acoustic bandwidth, sensitivity, sensing range, or deployment complexity. In several cases, coexistence with communication signals required sacrificing valuable optical bandwidth [8], [12], while others relied on dedicated or non-standard fiber infrastructures [5], [13].

Addressing these limitations requires the development of DAS architectures that can seamlessly integrate into existing

Manuscript created in July 2026. All authors are with LTCI Lab, Télécom Paris, Institut Polytechnique de Paris, 19 place Marguerite Perey, 91120 Palaiseau, France. (Corresponding author: elie.awwad@telecom-paris.fr)

telecommunication networks while preserving their operational constraints. Such systems should ultimately minimize additional infrastructure and equipment requirements to enable cost-effective and low-footprint deployment, exploit richer signal information to improve sensing sensitivity and coverage, mitigate the impact of noise through advanced signal processing and estimation techniques, and efficiently process the massive data streams generated by distributed sensing. This paper addresses several of these key challenges and presents solutions developed toward practical large-scale deployment of DAS over telecommunication infrastructures. The proposed approaches are illustrated through representative experimental demonstrations, highlighting their potential for enabling wide-area sensing using existing fiber-optic communication networks.

The main contributions of this work are fourfold. First, we review a few DAS classifications and we focus on recently proposed constant-amplitude continuous-wave DAS interrogators that enable in-band coexistence between distributed acoustic sensing and optical data transmission over the same deployed telecommunication fiber. Second, we investigate the influence of the mechanical coupling between the optical fiber, its hosting cable, and the surrounding environment on the interpretation of differential-phase measurements in terms of distributed strain. Using DAS data acquired during a recent field trial [15], we demonstrate that the fiber-to-ground coupling can exhibit significant spatial variations along deployed telecommunication fibers. Third, we show how polarization diversity can be exploited not only to mitigate polarization fading in DAS interrogators but also to measure distributed birefringence variations. Experimental results illustrating both static and dynamic birefringence changes are presented using a polarization-diversity DAS system. Finally, we analyze the impact of laser phase noise on continuous-wave, constant-power DAS interrogation based on phase-encoded probing sequences through a comparative numerical study that quantifies the influence of the probing sequence type and length on sensing performance.

The remainder of this paper is organized as follows. Section II reviews DAS interrogators in general and focus on continuous-wave DAS interrogators for in-band sensing and communication coexistence. Section III investigates the effect of the fiber mechanical coupling on distributed strain measurements. Section IV presents the use of polarization diversity for extracting distributed birefringence variations. Section V analyzes the impact of laser phase noise on phase-encoded continuous-wave DAS interrogation. Finally, Section VI concludes the paper.

II. Coexistence With Communication and Adaptation to Network Topology

DAS has evolved into a broad family of interrogation techniques that differ in their probing strategy, detection architecture, and the physical quantity extracted from the Rayleigh backscattered signal. Although these techniques rely on the same distributed scattering process, they exhibit distinct trade-offs in terms of spatial resolution, sensing bandwidth, sensitivity to strain, implementation complexity, and compatibility with deployed telecommunication networks. Hence, we start this section with brief classifications of DAS techniques before discussing coexistence of DAS with data transmission.

A. Receiver-based classification

A first classification can be done based on the receiver architecture. Direct-detection (DD) systems recover only the intensity of the beating terms resulting from the Rayleigh-backscattered signal portions unless an interferometric process between the backscattered signal and a time-delayed version of it or a reference signal is performed before the detection [16]. In contrast, coherent detection preserves both amplitude and phase of the optical field, enabling the extraction of distributed phase variations induced by external perturbations. It also offers important sensitivity gains compared to direct detection. In its polarization-diversity version, coherent detection can also mitigate polarization fading that occurs when the state of polarization (SoP) of the backscattered signal and the SoP of the local oscillator are not aligned [17], [18].

B. Probing-based classification

A second classification can be established according to the probing strategy. Conventional differential-phase-sensitive optical time-domain reflectometry ($\Delta\phi$-OTDR) relies on short optical pulses for probing and estimates the local optical phase from the time-resolved Rayleigh backscattered signal. Localization of a strain event is then performed by computing the differential phase variations between two segments in the fiber separated by the so-called 'gauge length'. Pulse-based interrogation naturally provides spatial localization through time-of-flight measurements but suffers from the well-known trade-off between pulse duration, spatial resolution, sensitivity (i.e. the smallest detectable strain change observed by the propagating optical signal), sensing range (i.e. the maximum fiber length covered by DAS), and mechanical bandwidth. It also suffers from nonlinear effects at high peak power and limited dynamic range due to phase unwrapping issues when the optical phase is locally disturbed by large strains. An alternative to the conventional $\Delta\phi$-OTDR that addresses the dynamic range issue is the chirped-pulse ϕ-OTDR that moves the dynamic strain detection from a phase-based to a time-delay-based measurement [19].

Moreover, several other evolutions of the conventional $\Delta\phi$-OTDR were also proposed and studied to enhance sensitivity. We will cite two evolutions: first, the use of multi-frequency pulses to mitigate coherent fading [20], [21], and second the use of linear-frequency-modulated (LFM) pulses that were also called time-gated OFDR (Optical Frequency Domain Reflectometry) or even OPCR (Optical pulse compression reflectometry) and chirped-pulse DAS [22]–[25] in which the spatial resolution is determined by the sweeping range of the LFM pulses rather than the pulse width. These LFM-pulse-based approaches help in enhancing the sensitivity and are very closely related to the schemes that will be introduced next. Alternatively, continuous-wave DAS probing techniques can be used to illuminate the fiber continuously (in contrast to pulsed-based probing) using deterministic probing

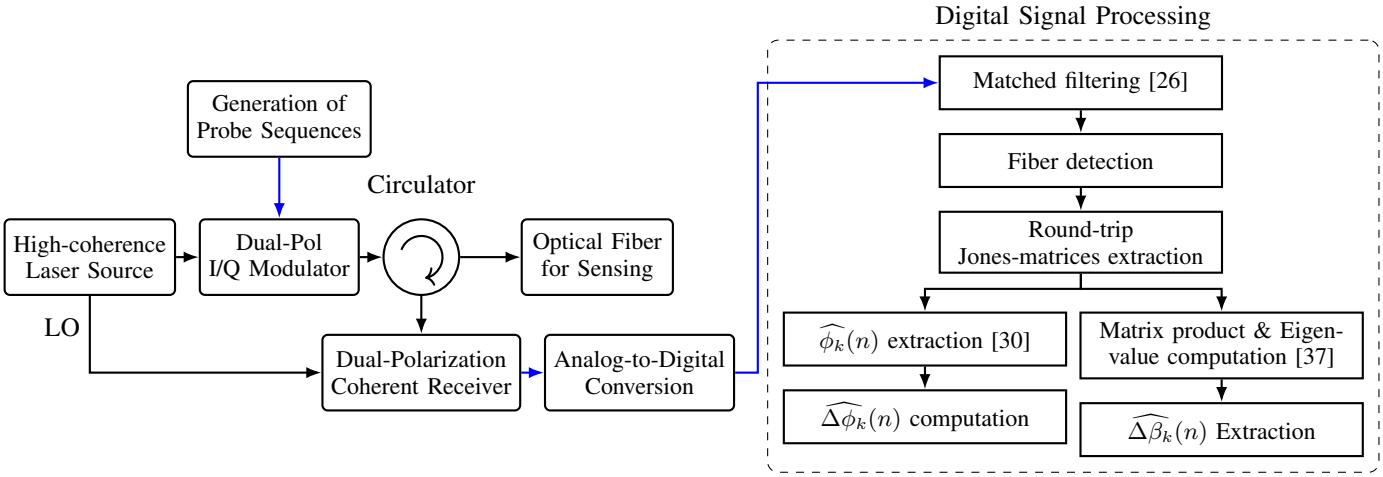

Fig. 1. On the left, a block diagram of a dual-polarization DAS system (blue (resp. black) arrows for electrical (resp. optical) signals) and on the right, the main digital-signal-processing steps. (I/Q: in-phase and quadrature, LO: Local Oscillator, k is the spatial segment index and n is the time index, $\widehat{\phi_k}(n)$ (resp. $\widehat{\Delta\phi_k}(n)$) is the estimated absolute (resp. differential) phase of segment k at time n, $\widehat{\Delta\beta_k}(n)$ is the estimated local birefringence.)

sequences [26], [27], i.e. discrete modulated states such as phase-coded waveforms, or deterministic analog signals such as frequency sweeps also know as OFDR (Optical Frequency Domain Reflectometry) [28], [29]. For both LFM-pulse-based DAS and continuous-wave DAS, spatial information is recovered through a correlation process, also referred to as a matched filtering [25], rather than through pulse propagation, enabling an important sensitivity enhancement while maintaining distributed measurements and avoiding the increase of the pulse peak power. Finally, dual-polarization probing was introduced in DAS [30] enabling an additional sensitivity enhancement and offering richer sensing capabilities as we will see in section IV. We illustrate in the left part of Fig. 1 the general scheme of a dual-polarization DAS probing system using I/Q-modulated continuous-wave probing sequences.

C. Coexistence of DAS and communication over a single unrepeatered link

A single DAS interrogator can monitor tens or even more than a hundred kilometers of silica optical fibers at a meter-scale spatial resolution and without the use of inline amplification [24]. Two main deployment scenarios are typically studied over telecommunication optical networks. On one hand, so-called 'dark fibers' provide a relatively straightforward deployment of conventional DAS techniques and have already been employed in several field trials. On the other hand, lit fibers allow sensing over operational communication links, avoiding the need for dedicated fiber resources. However, this deployment scenario requires strict coexistence between sensing and communication signals, imposing constraints on optical power, spectral allocation, and network compatibility to preserve the quality of transmission (QoT) [31]. In [9], in-band sensing and communication was achieved over a link of 80km with no impact on communication performance. For sensing, a wavelength was dedicated and modulated with a constant-power (< 0 dBm) continuous-wave DAS probe using polarization-multiplexed Golay-encoded sequences [26] along with polarization-diverse coherent detection. The scheme corresponds to the one shown on the left of Figure 1. The sensing wavelength was multiplexed within a C-band WDM transmission signal with no more than a 2 GHz spacing. Pulsed-based DAS interrogation struggles in achieving a similar performance due to the inherent nonlinear interference between the high-peak-power DAS signal and the neighboring communications signals [31].

Within this coexistence framework, the continuous-wave constant-power DAS shown in Figure 1 occupies an intermediate position between conventional $\Delta\phi$-OTDR and OFDR. Like coherent $\Delta\phi$-OTDR, it relies on coherent detection of Rayleigh backscattering to monitor distributed phase variations over long fiber spans. However, instead of using isolated optical pulses, the fiber is continuously illuminated with coded waveforms and the distributed response is reconstructed digitally through matched filtering. In this respect, the interrogation principle closely resembles OFDR, where the distributed impulse response of the fiber is also recovered from a continuously transmitted probing signal using coherent signal processing. Both approaches exploit long observation times, matched filtering, and digital reconstruction to maximize the collected backscattered energy, differing primarily in the choice of the probing waveform and the domain in which the matched filtering is performed: optical or digital. Continuous-wave phase-encoded DAS interrogation was revisited by several research groups and was referred to using different names such as spread-spectrum DAS, coded DAS, linear-frequency-modulated (or -swept) DAS, chirp-compression DAS or even chirped OFDR [9], [14], [24], [30], [32]. In all these works, the underlying concept is the same: they are essentially linear system identification problems in which the fiber can be viewed as a distributed linear filter characterized by its complex-valued Rayleigh reflectivity. OFDR estimates the impulse response of the fiber by probing the frequency response typically with a swept laser, whereas continuous-wave phase-coded DAS estimates the same impulse response by probing the

fiber with encoded waveforms and applying correlation in the digital domain. Their key advantage compared to pulsed DAS techniques is the resource-efficient integration over lit fibers with a highly-reduced nonlinear interference.

D. DAS deployement over an optical network

Finally, DAS systems still need to overcome challenges imposed by the topologies of the optical communication networks. Two examples are briefly given to illustrate these challenges. First, DAS operation through repeatered links is still impractical except over submarine optical links whose architecture enables several options for DAS integration without the filtering of the backscattered signals by the isolators in the amplification stages [14], [33]. Second, branching structures such as ROADMs, multiplexers and splitters bring additional problems for backscatter-based distributed sensing because these components will severely attenuate sensing signals and complicate event localization and system calibration. Recent works started addressing these issues in passive-optical-network (PON) scenarios using fast switching [11] or wavelength and code orthogonality [10], [34].

III. Fiber–Environment Coupling and Sensing Fidelity

A fundamental challenge in using deployed telecommunication fiber cables is the variability of the coupling between the fiber cable and its surrounding media. Unlike dedicated sensing installations, telecommunication cables come in various configurations that are designed to limit the mechanical coupling to the surrounding media. They are also installed using diverse methods and paths, leading to non-uniform mechanical coupling along the cable. Recently, Orange Labs offered us the opportunity to perform DAS measurements on a deployed telecommunication cable in Lannion [15]. The cable is a Prysmian L1091-14 containing 72 G.657 single-mode fibers with a total length of 1145 m, as seen on Fig. 2. It is installed as shown in Fig. 3, with the first 64 m (in pink) laying on the ground surface, followed by two loops of 540 m that are underground (first loop in black and second loop in red). For the two loops, we used two optical fibers in the same module in the same optical cable. The coupling of the cable with the surrounding media is not controlled and cannot be checked. During this field trial, surface waves were measured, and collocated sensors were used to verify the DAS measurements. More details on the experiments can be found in [15].

As a first conclusion, we noted that a quantitative strain-amplitude measurement is a real challenge. The strain value in the surrounding medium can be different from the one measured in the glass fiber through DAS due to the impact of the coupling between the medium, the cable and the sensing fiber within the cable. A promising metric to characterize the quality of the coupling between the optical fiber and the medium is the coherency metric introduced in [35]. The coherency is a metric that compares neighboring DAS channels (i.e. fiber segments) to identify the ones that are observing - or not - the same strain variations. Its use is relevant when the observed mechanical

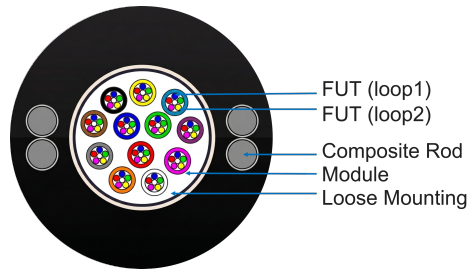

Fig. 2. Cross section of the 72-fiber (SMF-G657) Prysmian L1091-14 cable.

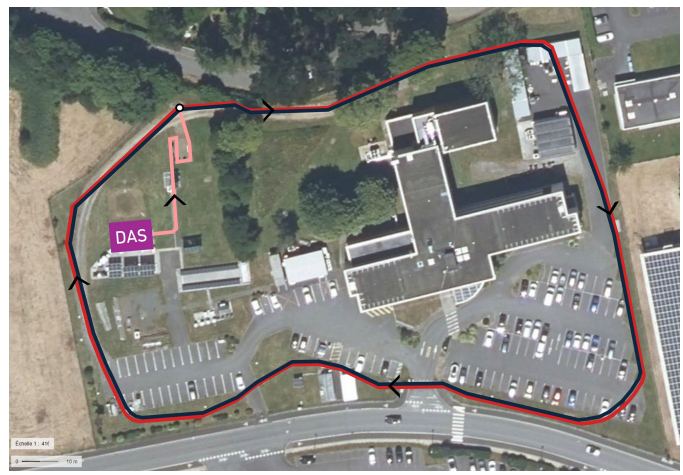

Fig. 3. Orange Lab test field: FUT (Fiber Under Test) layout featuring a first section on the ground (in pink) followed by a first loop (in black), and a second loop (in red).

perturbations have wavelengths λ_{meca} that are greater than twice the gauge length, denoted Δz. In this case, the two neighboring DAS channels should measure the same strain perturbation. In the next paragraph, we explain how we adapt the coherency metric to our DAS measurements.

Conventional DAS allows the extraction of differential phases $\widehat{\Delta\phi}_k(n)$, where n is the time index and $k \in [1, K]$ is the DAS channel index. To preserve the highest spatial granularity from our DAS data, we extract the differential phases using a gauge length equal to the native sampling resolution, 0.51 m in our case. This brings artifacts into the coherency calculations due to the well-know intensity-fading in DAS. Hence, pre-processing DAS data is required. First, $\widehat{\Delta\phi}_k(n)$ are zero-meaned over the slow-time dimension and are band-pass filtered with cut-off frequencies of 3 and 15 Hz to remove the slow variations, focusing on surface waves induced by anthropogenic or natural sources. After, the differential phases are cut into W time windows of T samples each with an overlap of 50%. For each time window, the differential phases are de-meaned and normalized by their Euclidean norm (Eq.(1)). Normalization is required to assess relative coupling as differential phased from successive channels may exhibiting different amplitudes. Then, we compute the cross-correlation between successive channels $\widehat{\Delta\phi}_k(w,t)$ and $\widehat{\Delta\phi}_{k+1}(w,t)$ (Eq.(2)) where $w \in [1, W]$ is the time-window index and t is a local time index in each window w. Finally, we keep the maximum correlation value (Eq.(3)).

$$\Delta\phi'_k(w,t) = \frac{\widehat{\Delta\phi}_k(w,t) - \frac{1}{T}\sum_{t=1}^{T}\widehat{\Delta\phi}_k(w,t)}{\sqrt{\sum_{t=1}^{T}\left(\widehat{\Delta\phi}_k(w,t) - \frac{1}{T}\sum_{t=1}^{T}\widehat{\Delta\phi}_k(w,t)\right)^2}} \quad (1)$$

$$r_k(w,\tau) = \sum_{t=\max(1,\,1-\tau)}^{\min(T,\,T-\tau)} \Delta\phi'_k(w,t)\Delta\phi'_{k+1}(w,t+\tau) \quad (2)$$

$$C_k(w) = \max_{\tau\in[-\tau_{\max},\,\tau_{\max}]} |r_k(w,\tau)| \quad (3)$$

where τ_{max} is considered for a surface wave with velocity $v_{\text{meca}} = 300$m/s, hence $-0.003\text{s} < \tau < 0.003\text{s}$ with $\tau = \Delta z / v_{\text{meca}}$. The absolute value operator is used to focus on the coupling strength and not its polarity. Hence, $C_k(w)$ only represents if adjacent channels are reacting the same to ambient surface waves without considering any phase inversion. For each DAS channel k, the computed coherency values are ranked and the best 90% windows are kept to reduce the impact of noise and transitory acoustic events in the measured windows. The number of kept windows is denoted n_{keep} and the formed set is denoted W_{keep}. From this subset, we calculate the mean coherency between adjacent channels as:

$$C(k) = \frac{1}{n_{\text{keep}}} \sum_{w\in W_{\text{keep}}} C_k(w) \quad (4)$$

16 five-second DAS recordings of ambient surface waves were performed during the Lannion field trial. The chosen window size is 1 second. Evaluating coherency using ambient acoustic noise is justified by the homogeneous energy distribution along the fiber, which allows the isolation of intrinsic inter-segment coupling from any coherence induced by a dominant local event. $C(k)$ is computed for each recording and the stacked $C(k)$ curve is shown on Fig. 4 in blue. We can clearly identify two average coherency levels. A first $\sim$ 60 m-long section shows a much lower coherency level than the rest of the link indicating a lower mechanical coupling with its surroundings. On-the-field observation of the link shows that the first 64 m-section is laying on the ground surface or suspended in a technical cabinet before entering into the ground. Hence, the computed coherency metric clearly identifies these two cable configurations. We also show on Fig. 4 a median-filtered version of the coherency metric through the dashed green curve.

Now, if we look more closely to the coherency levels of the underground sections of the link (Fig. 5 in which we superpose the coherency levels of the two loops) and recall that these sections consist of two fiber loops installed in the same module of the same optical cable, we notice that the two fibers show different coherency levels with their surroundings even if they follow the same path within the same module. However, we can locally identify DAS channels from the two loops showing similar coherency, for instance the channels around 120 m and 725 m, and also the channels around 137 m and 745 m. A few hypotheses to explain those observations are the existence of a torsion of the optical fiber cable exposing one fiber loop more than the other to the internal walls of the cable or the rearrangement of the optical fibers within the cable.

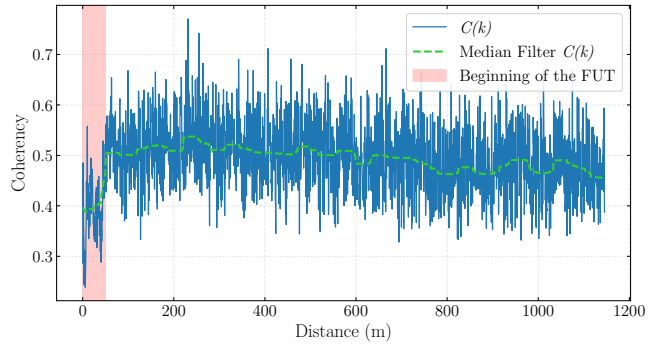

Fig. 4. Coherency between adjacent channels from the Lannion field trial.

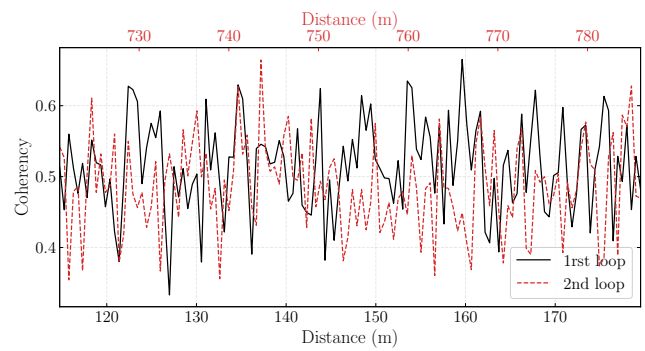

Fig. 5. Medium coupling coefficient, zoom on a portion of the optical fiber common to both loops.

From these preliminary coherency evaluations on an installed telecommunication cable, we spot a real challenge, but also an opportunity for further research, to assess the coupling of each optical fiber with its surroundings and understand the impact of all the involved elements on the DAS measurements, such as the cable installation, the loose/tight mounting of the fibers within the cable, the coating conditions, the topology and the ground material around the cable.

IV. Polarization Dynamics and Birefringence-Based Sensing

Conventional DAS systems rely on common optical phase measurements neglecting polarization dynamics. However, real-world perturbations can also induce changes in the local fiber's birefringence. A recent Multiple-Input-Multiple-Output (MIMO) DAS system enabled the extraction of both phase and polarization parameters along the fiber [30], however the main target was the mitigation of polarization fading effects. By further exploiting the estimated parameters for assessing the distributed linear birefringence strength, such DAS systems can detect and localize non-axisymmetric perturbations. Inspired from polarization-OTDR techniques mostly applied for static birefringence measurements [36], we recently investigated the use of polarization-diversity DAS and we proposed a numerical model of polarization dynamics in silica

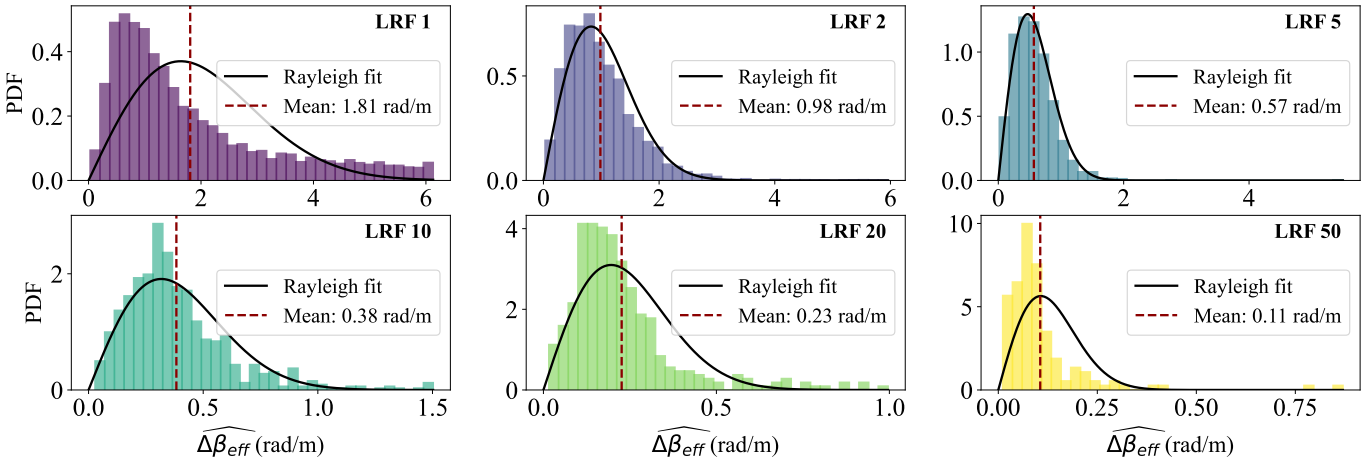

Fig. 6. Histograms of estimated birefringence $\widehat{\Delta\beta_{eff}}$ for different Low Resolution Factors (LRF).

fibers for DAS applications [37]. In this section, we experimentally demonstrate additional static and dynamic strain sensing capabilities. All details of the experimental setup can be found in [38].

We note the round-trip matrix from the fiber start to segment i and back $\hat{\mathbf{H}}_i^{rt}$, for $i \in [1, N_{seg}]$ with N_{seg} the total number of segments. In our setup, the sampling frequency at the DAS acquisition card is set to 400 MHz, yielding a native DAS channel length of 0.255 m. We send Golay codes of duration 0.163 ms (Golay order 12). To mitigate coherent fading and therefore avoid large estimation errors, we can select the highest reflecting segments among groups of segments of a given size, resulting in a non-uniform gauge length. Hereafter, we will denote the group size the Low Resolution Factor (LRF). The selected subset of segments J is of size $\lfloor N_{seg}/LRF \rfloor$. For each consecutive pair of selected segments (k, k') in J, we compute [39]–[41]:

$$\mathbf{T}_{k'} = (\widehat{\mathbf{H}}_k^{rt})^{\dagger} \widehat{\mathbf{H}}_{k'}^{rt} \tag{5}$$

Extracting the eigenvalues from this matrix product, we can compute an estimate of the effective retardance $\widehat{\Delta\beta_{eff}}L$ [38] (the phase shift between the two eigen-polarizations introduced by the propagation in the segment, due to the difference in refractive indices between the two modes), with $\widehat{\Delta\beta_{eff}}$ the estimated effective birefringence magnitude in rad/m and L the distance between k and k'. The birefringence $\widehat{\Delta\beta_{eff}}$ is an effective quantity that depends on the LRF.

When the local birefringence vector varies over length scales smaller than the distance between two selected segments, the estimated birefringence magnitude does not correspond to the local birefringence magnitude at a specific position. Instead, it results from the accumulation of the local birefringence contributions over the considered length, and depends on the relative orientations of the true local vectors. To illustrate this effect, we first performed measurements in static conditions over a 1958m fiber spool. Figure 6 shows the distribution of the effective birefringence magnitude for different LRF. When there is no selection, we observe a widespread distribution, that does not fit the expected Rayleigh distribution [42]. This can be explained by the strong effect of coherent fading: lowest reflecting segments lead to large errors in the estimated matrices, which are not reliable. For LRFs of 2 and 5, we see that the distributions better show the expected behavior. However, for higher LRFs, the distributions tend to deviate from a Rayleigh. We observe that as the LRF (and consequently the gauge length) increases, the mean value of the estimated birefringence decreases. This effect has been observed in [43] and might be explained by the fiber being spun. Indeed, the propagation over the gauge length can be viewed as the composition of successive polarization rotations on the Poincaré sphere. The equivalent rotation angle is always smaller than or equal to the sum of the individual rotation angles, with equality only when all local birefringence vectors are aligned. Consequently, changes in birefringence orientation reduce the magnitude of the effective birefringence relative to the true local birefringence. Therefore, the choice of the LRF is a trade-off between coherent fading mitigation and accurate birefringence estimation. Since the estimated birefringence depends on the spatial resolution in this case, it is more interesting to study relative trends than absolute values. Hence, we performed a measurement over the 1958 m fiber spool followed by a 235 m fiber spool. Figure 7 shows the birefringence estimation for different LRFs as a function of distance in the fiber. A moving spatial average of window size 25 was applied to smoothen the traces and highlight the main trends. On the traces, we can observe the transition from the first fiber spool to the second, especially for LRFs 5 and 10. For a LRF of 2, the trace is still quite noisy, making the transition less clear, and for 20, the averaging becomes too large to see a sharp transition. Thus, the choice of the LRF needs to be tailored depending on the application.

Finally, to assess the ability to detect dynamic events through birefringence estimation, we placed a fiber squeezer between the 1958m spool and 235m spool. This device compresses the fiber between two parallel plates to induce birefringence changes through a transverse force. Indeed, birefringence changes mainly occur from anisotropic strains that break the cylindrical symmetry. Figure 8 shows the effective

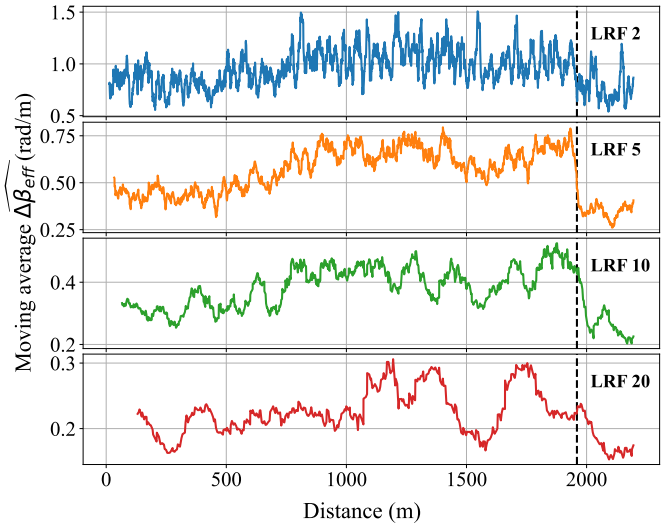

Fig. 7. Effective birefringence magnitude $\widehat{\Delta\beta_{eff}}$ versus distance for different LRFs and with a moving spatial average of 25 segments. The transition between the two spools is marked by the red vertical line.

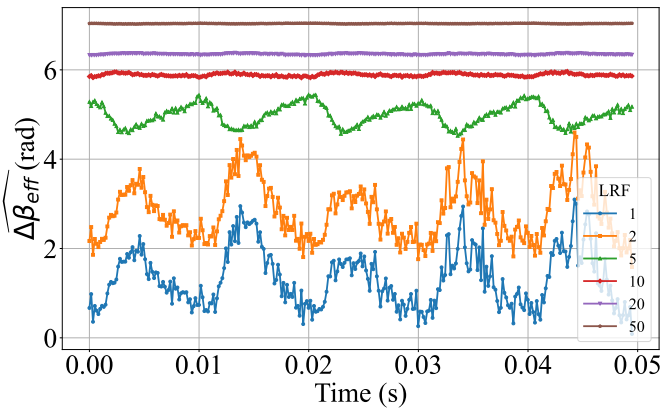

Fig. 8. Effective birefringence estimation at event location versus time for different LRFs, with added offsets to separate the traces.

birefringence magnitude estimated at the event location for different LRFs versus time, with added offsets for better visualization. We see that for LRFs of 1 and 2, the birefringence evolution has different shape and magnitude than for a LRF of 5 since the event signature is less mixed with adjacent segments that may have different birefringence orientation and magnitudes, and therefore reduce the contribution from the perturbed segments. Here, the two traces for LRF 1 and 2 are the exact same ones: indeed, since the segment selection step selects the most reflective among 2 segments, sometimes two consecutive segments might be selected and therefore the birefringence estimation be the same as in the no-selection case for this particular fiber location. Moreover, we observe that the event signature is almost unnoticeable on higher LRFs.

V. Phase Noise Limitation

Laser phase noise is a fundamental limitation in coherent DAS systems [44], especially when applied over long fiber spans or when an encoded-DAS or chirped-DAS interrogation along with matched-filtering is used [25]. Phase noise directly impacts the accuracy of channel estimation and the reliability of extracted phase and polarization parameters. Understanding and mitigating phase noise is therefore essential for next-generation coded DAS systems targeting long-range sensing over deployed telecom fibers with telecom-grade components. In this context, we present a comparative numerical study of coded sequences to assess their phase noise resilience when using a MIMO DAS system.

A. Studied probing sequences

For this study, we select several sequence families employed in coded DAS systems: Golay complementary pairs [26], Legendre sequences [27], maximum length sequences (m-sequences) [17], and Constant Amplitude Zero Auto-Correlation (CAZAC) sequences [32]. Within the CAZAC family, we consider two variants: the Perfect-Square Minimum-Phase (PS-MP) sequence and Zadoff–Chu sequences [45], [46].

Periodic autocorrelation is a key performance indicator for sequences employed in DAS systems. Among the selected families, Golay and CAZAC sequences provide perfect periodic autocorrelation zones, enabling ideal channel estimation, whereas Legendre and m-sequences exhibit non-perfect periodic autocorrelation (they tend to perfect when their length tends to infinity).

Beyond periodic autocorrelation, we introduce the concept of frequency diversity, which we define as a measure of how broadly the energy of a sequence is spread across frequencies, to characterize the sequences in the spectral domain. Three Zadoff–Chu sequences are selected, exhibiting maximum, intermediate, and minimum frequency diversity, respectively. The PS-MP CAZAC sequence presents a narrow frequency diversity. All remaining sequences (Golay, Legendre and m-sequences) exhibit an approximately uniform spectral distribution, corresponding to a broad frequency diversity. The spectrograms of these sequences and the notion of frequency diversity are further explored in [47]. As shown below, this distinction in frequency diversity translates into observable differences in phase noise resilience.

Several practical distinctions between the sequence families should be noted. CAZAC sequences are composed of many discrete unit-norm and complex-valued symbols, which increases their hardware implementation complexity because a very accurate I/Q electro-optic modulator would be needed to generate them. Among them, only the PS-MP CAZAC sequence can be directly mapped onto Phase Shift Keying (PSK) modulation. All remaining families are binary. Furthermore, only Golay sequences provide two distinct mutually orthogonal pairs, one per polarization; for all other families, orthogonality between polarizations is obtained by cyclically shifting the sequence transmitted on the second polarization by half the sequence length [32]. Finally, the sequences cannot be constructed for arbitrary lengths if their autocorrelation properties are to be preserved, which constrains the code lengths available to each family.

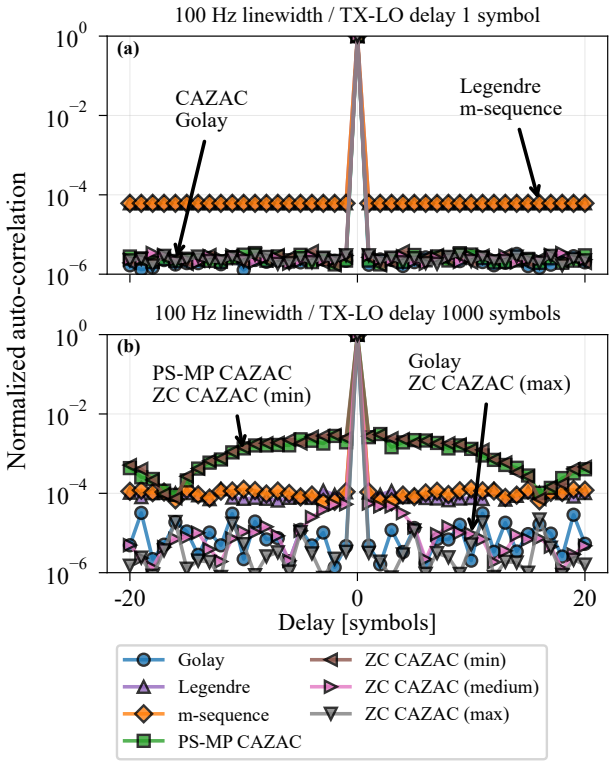

Fig. 9. Correlation of each of the considered coded sequences with its phase-noise-affected counterpart, zoomed around the correlation peak, for a 100 Hz laser linewidth and a TX–LO delay of (a) 1 symbol and (b) 1000 symbols. In (b), the intermediate-diversity ZC CAZAC sequence lies between the two labelled groups.

B. Initial back-to-back study with time delay

Before evaluating the sequences within the DAS simulation framework, we investigate the effect of phase noise on the sequence correlation properties. To this end, the correlation is computed between the original undisturbed sequence, $s[n]$, and its phase-noise-impaired counterpart,

$$s'[n] = s[n]e^{j\phi_{TX}[n]}e^{-j\phi_{LO}[n]} = s[n]e^{j(\phi[n]-\phi[n-d]}), \quad (6)$$

where $\phi_{\mathrm{TX}}[n]$ and $\phi_{\mathrm{LO}}[n]$ denote the transmitter (TX) and local oscillator (LO) phase noise, respectively. Since both originate from the same laser, following a random-walk process $\phi[n]$, they differ only by the round-trip delay d. Although this scenario corresponds to a back-to-back configuration without fiber propagation, the TX–LO delay can be related to the round-trip delay of the different fiber segments: shorter delays represent segments closer to the interrogator, while longer delays correspond to more distant points along the fiber. Two delays of 1 and 1000 symbols are considered, both much shorter than the sequence length which is approximately 16384 symbols, with slight differences per sequence.

Fig. 9(a) shows the normalized correlation for a 100 Hz FWHM laser linewidth and a 1-symbol TX–LO delay. Legendre and m-sequences exhibit sidelobes at approximately 6×10^{-5}, a level set by their non-perfect autocorrelation and already present in the absence of phase noise. Golay, PS-MP CAZAC and ZC CAZAC sequences, in contrast, lose their perfect autocorrelation and develop sidelobes of the order of 10^{-6}, still more than one order of magnitude below the non-perfect autocorrelation families.

For the 1000-symbol delay in Fig. 9(b), the degradation becomes considerably more pronounced and a clear ordering emerges. Legendre and m-sequences remain close to their phase-noise-free level, while PS-MP CAZAC and the minimum-diversity ZC CAZAC sequence exhibit the highest sidelobes, exceeding 10^{-3}. Golay and the maximum-diversity ZC CAZAC sequence show the lowest levels, with the intermediate-diversity ZC CAZAC sequence lying in between. This ordering follows the frequency diversity of the sequences. These results indicate that a higher frequency diversity provides robustness against phase-noise-induced degradation of the channel estimation.

C. Numerical study over a sensing fiber

To evaluate the performance of these sequences on the MIMO DAS framework, simulations are performed at a symbol rate of 50 Mbaud over a 2 km fiber, corresponding to 2 m segments, with variable code lengths. Each configuration is repeated for 10 independent Rayleigh-distributed fiber profiles, and the reported results correspond to the average across all realizations. Differential phases are extracted following the DSP steps shown in the right part of Figure 1. Phase errors are evaluated with respect to the ground-truth values available in simulations, after selecting one out of every ten scatterers based on the reflectivity, resulting in an effective gauge length of approximately 20 m.

Fig. 10(a) shows the phase error for each sequence as a function of code length when phase noise is excluded from the simulation framework. For the shortest code lengths, all sequences exhibit large errors, since the code duration is shorter than twice the channel spreading time of the fiber, $2T_{ir}$, which is the minimum required for full Jones matrix estimation of the round-trip propagation. As the code length increases, the errors decrease. CAZAC sequences are the first to do so, owing to their perfect autocorrelation properties; note that all CAZAC variants yield overlapping results in this scenario, and that PS-MP CAZAC sequences exist only for perfect-square lengths, restricting them to powers of four on the simulated grid, which explains the missing points for this sequence. Golay codes also possess perfect autocorrelation; however, they require code lengths of at least $4T_{ir}$ in order to avoid aliasing with their non-zero autocorrelation zone, beyond which their performance coincides with that of the CAZAC sequences. The remaining sequences, Legendre and m-sequences, whose results also overlap, show errors that decrease with code length at a slower rate, as a consequence of their non-perfect autocorrelation properties.

Fig. 10(b) shows the corresponding results when phase noise from an ultra-narrow-linewidth laser of 10 Hz FWHM linewidth is included. Two effects are observed. First, the error reduction with code length slows down considerably; as a consequence, the advantage of perfect autocorrelation

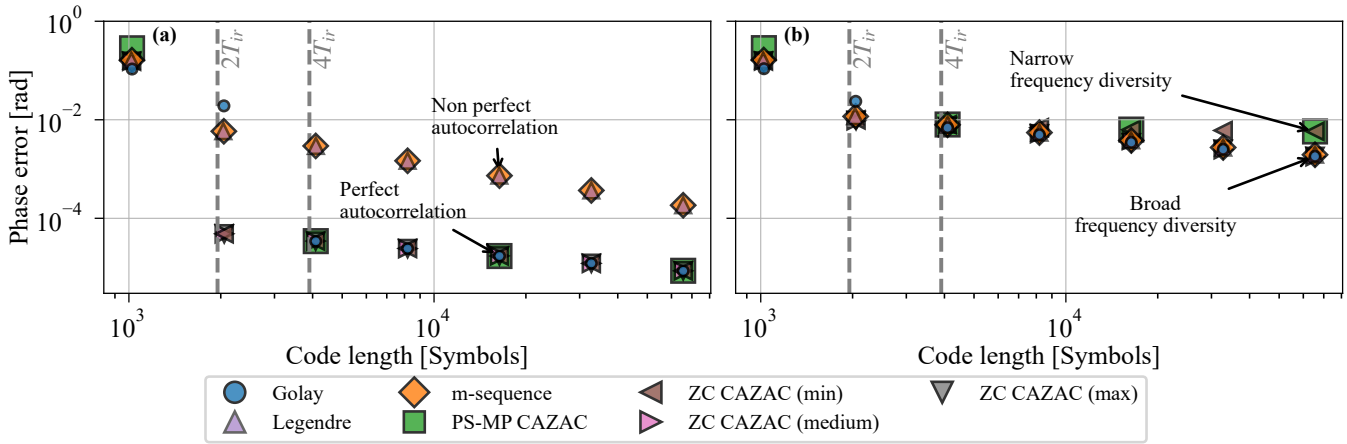

Fig. 10. Phase estimation error versus code length for the considered sequences, simulated over a 2 km fibre (a) without phase noise and (b) with phase noise corresponding to a 10 Hz laser linewidth. Vertical dashed lines mark twice and four times the channel spreading time of the fiber, $2T_{ir}$ and $4T_{ir}$.

largely vanishes, and all sequence families converge towards a similar error level. Second, a distinct behaviour emerges depending on the frequency diversity of each sequence: the PS-MP CAZAC and minimum-diversity Zadoff–Chu sequences, both with narrow frequency diversity, reach an error approximately three times higher than that of the sequences whose energy is spread broadly across the spectrum (5.7×10^{-3} versus 1.8×10^{-3} rad at the largest considered code length). This behavior is consistent with the back-to-back correlation results of Fig. 9(b) and may be attributed to an averaging effect: spreading the sequence energy over a wider frequency range averages the phase-noise-induced distortion across the spectrum, benefiting the estimation as was observed for Golay codes in [32]. These results indicate that autocorrelation quality governs performance in the noise-limited regime, whereas frequency diversity becomes a decisive sequence property once phase noise dominates.

D. On laser phase noise compensation

Even when the sequence most resilient to phase noise is selected, performance degradation cannot be avoided. In such cases, phase noise compensation becomes necessary. Most existing compensation techniques, however, entail an increase in hardware complexity: recent works have focused on enhancing the phase stability of the laser source [48], while others measure the phase noise with an auxiliary coherent receiver and subsequently subtract it from the main sensing signal [49]. Although effective, these approaches introduce additional hardware and cost. This motivates the investigation of phase noise estimation and compensation based purely on digital signal processing, requiring no additional hardware.

We address phase noise compensation through a joint scheme combining a Kalman filter for phase noise estimation with least-mean-squares (LMS) MIMO channel estimation [50], replacing the first three steps of the digital signal processing block in Fig. 1: matched filtering, fiber detection, and round-trip matrix extraction. Once the fiber has been detected, which can still be performed by matched filtering, the two estimators operate jointly on a per-sample basis: for each received sample, the Kalman filter first predicts the current phase noise; this prediction is used to de-rotate the sample before the LMS channel update; finally, the Kalman state is updated from the residual phase deviation before the next sample is processed. Since the local oscillator is derived from the same laser and constitutes a delayed replica of it, a single phase noise process suffices to describe both transmitter and local-oscillator contributions, provided the delay is known; the Kalman filter therefore estimates only this single process.

To evaluate this approach, we perform simulations over a range of laser linewidths, comparing the cases with and without phase noise compensation. For the same 2 km fiber as before, Golay complementary pairs of 4096 symbols are transmitted, and the results are averaged over 5 independent Rayleigh-distributed fiber realizations. The simulations are performed under static conditions, i.e., without applied strain events, so that any residual variation in the estimated channel originates from phase noise alone. The LMS step size is set to 0.1, chosen as a compromise: since both estimators operate jointly, a faster adaptation would allow the LMS to absorb part of the phase noise into the channel estimate, degrading the recovered sensing phase, while a slower one would limit the tracking of channel variations. Its optimization, and the evaluation under dynamic conditions, are left for future work.

Fig. 11 shows the resulting phase error as a function of laser linewidth, together with the phase-noise-free baseline (dashed line). The per-sample tracking of the Kalman filter is beneficial over the entire linewidth range, with the compensated error remaining approximately a factor of five below the uncompensated case. The residual gap to the phase-noise-free baseline reflects the estimation noise of the filter, which prevents perfect phase recovery even at the lowest linewidths. Above approximately 10 kHz, the phase evolves too rapidly for the filter to track accurately and the benefit progressively narrows, until both cases converge, at linewidths beyond $\sim$100 kHz.

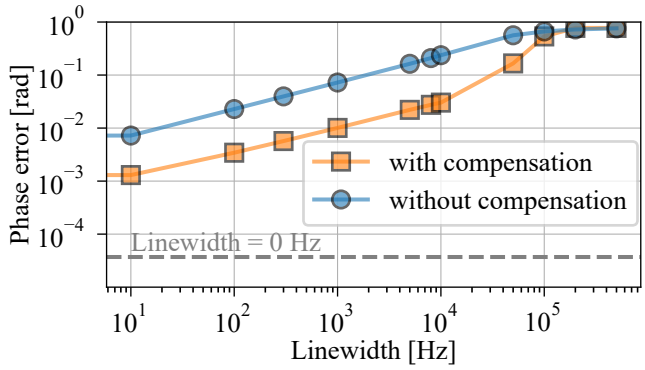

Fig. 11. Phase error as a function of laser linewidth using Golay complementary pairs of 4096 symbols over a 2 km fiber. In the compensated case, the phase noise is estimated by a Kalman filter operating jointly with LMS MIMO channel estimation. The dashed line indicates the phase-noise-free baseline.

VI. Conclusion

Distributed fiber sensing over deployed networks has the potential to transform these networks into pervasive monitoring platforms. In this paper, we shed light on major challenges facing the deployment of DAS over telecommunication networks. We focused specifically on three challenges: the extraction of quantitative longitudinal strain measurements, the extraction of birefringence measurements from MIMO DAS and the impact of laser phase noise on continuous-wave phase-encoded DAS. We briefly describe a few opportunities to address these challenges. For the first, the coupling of the sensed fiber with its surrounding medium could be used to calibrate the extracted strain, offering a complementary tool to propagation delays or frequency-wavenumber $(f-k)$ metrics. For the second, while the proposed method allows anisotropic transverse strain detection, the event characterization depends on the chosen spatial resolution. Hence, a multi-resolution approach can help in better understanding the detected strains. For the third, we observed that autocorrelation and frequency diversity properties must be considered in sequence selection for coded DAS systems as well as for other continuous-wave interrogation strategies based on frequency sweeps. Moreover, digital signal processing-based phase-noise compensation could enable the use of lasers with larger linewidth, and therefore lower cost, by relaxing the phase noise requirements for a given target performance. The scheme illustrated in this paper is only one possible realization, and the residual estimation-noise floor and high-linewidth tracking limit leave room for improvement through other estimation and compensation approaches.

Future research is expected to focus on design of new network-compatible sensing architectures, further integration of joint sensing and communication, and management of data volumes from large-scale sensing over operational networks.

Acknowledgments

Our research works received funding from ANR (Agence Nationale de la Recherche) within the SAFER project (grant ANR-24-CE42-3114), from AID (Agence Innovation Défense) within the FIBROUS project, and from IMT (Institut Mines-Télécom) within the FRAME-XG program.

References

[1] N.J. Lindsey, et al. "City-scale dark fiber DAS measurements of infrastructure use during the COVID-19 pandemic," *Geophysical Research Letters*, vol. 47, 2020. 10.1029/2020GL089931

[2] T. Li, et al. "Field Tests of AI-Driven Road Deformation Detection Leveraging Ambient Noise over Deployed Fiber Networks," in *Proc. of OFC*, 2025. 10.1364/OFC.2025.M1C.6

[3] V. Sharif, et al. "Urban Water Leakage Detection System based on Distributed Acoustic Sensing over Dark Fiber Networks," in *Proc. of OFC*, 2025.10.1364/OFC.2025.Th1I.7

[4] P. Tovar, et al. "Fiber layout inference via environmental acoustic noise similarity: A field trial," in *Proc. of OFC*, 2026. 10.1364/OFC.2026.M1I.2

[5] G. Cedilnik, et al. "Pushing the Reach of Fiber Distributed Acoustic Sensing to 125 km Without the Use of Amplification," *IEEE Sensors Letters*, 3(3), 2019.10.1109/LSENS.2019.2895249

[6] T. Zhu, et al. "Sensing Earth and environment dynamics by telecommunication fiber-optic sensors: an urban experiment in Pennsylvania," *Solid Earth*, vol.12, 2021. 10.5194/se-12-219-2021

[7] J.B. Ajo-Franklin, et al. "Distributed Acoustic Sensing Using Dark Fiber for Near-Surface Characterization and Broadband Seismic Event Detection," *Sci Rep*, vol. 9, 2019. 10.1038/s41598-018-36675-8

[8] M. Huang, et al. "First Field Trial of Distributed Fiber Optical Sensing and High-Speed Communication Over an Operational Telecom Network," in *J. Lightwave Technol.*, 38(1), 2020. 10.1109/JLT.2019.2935422

[9] S. Guerrier, et al. "Vibration Detection and Localization in Buried Fiber Cable after 80km of SSMF using Digital Coherent Sensing System with Co-Propagating 600Gb/s WDM Channels," in *Proc. of OFC*, 2022. 10.1364/OFC.2022.M2F.3

[10] P. K. Choudhury, et al. "Wavelength and Code Orthogonality Based Distributed Acoustic Sensing over a Passive Optical Network," in *Proc. of OFC*, 2025. 10.1364/OFC.2025.W3J.3

[11] H. Takahashi, et al. "Simultaneous monitoring of 8 fiber routes by means of high-speed switching for time-sharing FDM-DAS," in *Proc. of OFC*, 2025. 10.1364/OFC.2025.Th1I.2

[12] Y.-K. Huang, et al. "Field Trial of Coexistence and Simultaneous Switching of Real-time Fiber Sensing and 400GbE Supporting DCI and 5G Mobile Services," in *Proc. of OFC*, 2023. 10.1364/OFC.2023.W3H.4

[13] P. S. Westbrook, et al. "Enhanced Backscatter Fibers for Sensing in Telecom Networks," *J. Lightwave Technol.*, vol. 41, 1010–1016, 2023.10.1109/JLT.2022.3225750

[14] M. Mazur, et al. "Submarine Cable Deep-Ocean Observation of Mega-Thrust Earthquake and Tsunami with 44,000 100-m Spaced Sensors," in *Proc. of ECOC*, 2025.10.1109/ECOC66593.2025.11263003

[15] P. Pruvost, et al. "Frequency-Domain Characterization of Deployed Fiber-Medium Coupling using DAS," in *Proc. of OFC*, 2026.10.1364/OFC.2026.Th2A.59

[16] A. Hartog, "An introduction to distributed optical fibre sensors', Chapter 6, Sections 6.2 and 6.3, *CRC press*, 2017.

[17] H. F. Martins, et al. "Real time dynamic strain monitoring of optical links using the backreflection of live PSK data," *Opt. Express*, vol. 24, 2016.10.1364/OE.24.022303

[18] Q. Yan, et al. "Coherent ϕ-OTDR based on polarization-diversity integrated coherent receiver and heterodyne detection," in *Proc. of OFS*, 2017.10.1117/12.2265463

[19] J. Pastor-Graells, et al. "Single-shot distributed temperature and strain tracking using direct detection phase-sensitive OTDR with chirped pulses," *Opt. Express*, vol. 24, 2016.10.1364/OE.24.013121

[20] M.J. Murray, et al. "Quantitative amplitude-measuring ϕ-OTDR with $\mathrm{p}\epsilon/\sqrt{\mathrm{Hz}}$ sensitivity using a multi-frequency pulse train," *Opt. Lett.*, vol. 45, 2020.10.1364/OL.400159

[21] Y. Wakisaka, et al. "Proposal and real-field demonstration of large-scale vibration monitoring by using multi-frequency ϕ-OTDR distributed acoustic sensing," in *Proc. of ECOC*, 2023.10.1049/icp.2023.2049

[22] Wei. Zou, et al. "Optical pulse compression reflectometry: proposal and proof-of-concept experiment," *Opt. Express*, vol. 23, 2015.10.1364/OE.23.000512

[23] S. Wang, et al. "Distributed fiber-optic vibration sensing based on phase extraction from time-gated digital OFDR," *Opt. Express 23*, vol. 23, 2015.10.1364/OE.23.033301

[24] O. H. Waagaard, et al. "Real-time low noise distributed acoustic sensing in 171km low loss fiber," *OSA Continuum*, vol.4, 2021.10.1364/OSAC.408761

[25] E. Ip, et al. "DAS Over 1,007-km Hybrid Link With 10-Tb/s DP-16QAM Co-Propagation Using Frequency-Diverse Chirped Pulses," *J. Lightwave Technol.*, vol. 41, 2023.10.1109/JLT.2022.3219369

[26] C. Dorize and E. Awwad, "Enhancing the performance of coherent OTDR systems with polarization diversity complementary codes," *Opt. Express*, vol. 26, 2018.10.1364/OE.26.012878

[27] J. J. Mompó, et al. "Distributed dynamic strain sensing via perfect periodic coherent codes and a polarization diversity receiver," *J. Lightw. Technol.*, vol. 37, 2019.10.1109/JLT.2019.2913464

[28] Lihi Shiloh, et al. "Sinusoidal frequency scan OFDR with fast processing algorithm for distributed acoustic sensing," *Opt. Express*, vol. 25, 2017.10.1364/OE.25.019205

[29] R. Ryf, et al. "Coexistence demonstration of reflective OFDR sensing and commercial transceivers in a submarine testbed," in *Proc. of OFC*, 2026.10.1364/OFC.2026.M4J.5

[30] S. Guerrier, et al. "Introducing Coherent MIMO Sensing, a fading-resilient, polarization-independent approach to phase-OTDR," *Opt. Express*, vol.28, 2020.10.1364/OE.396460

[31] J. Wang, et al. "Simulation and Experimental Studies of DWDM Nonlinear Phase/Polarization/Power Crosstalk Between DFOS and Communication Channels in 27.6Tb/s 800ZR Metro Network," in *Proc. of ECOC*, 2025.10.1109/ECOC66593.2025.11263210

[32] C. Dorize, et al. "Optimal probing sequences for polarization-multiplexed coherent phase OTDR," in *Proc. of OFS*, 2020.10.1364/OFS.2020.T3.23

[33] R. A. Colares, et al. "DAS over a 585-km EDFA-repeatered Link with Co-propagating 15.8-Tb/s Transmission," in *Proc. of OFC*, 2026.10.1364/OFC.2026.M4J.6

[34] G. Wang, et al. "High-Bandwidth Branch-Ambiguity-Free Probing for Single-Wavelength DAS in PON," accepted for presentation at ECOC, *HAL [Preprint]*, 2026.Available Online

[35] T. Hudson, et al. "Unlocking DAS amplitude information through coherency coupling quantification," *Seismica*, 2025.10.26443/seismica.v4i1.1488

[36] L. Palmieri. "Distributed polarimetric measurements for optical fiber sensing," *OFT*, vol.19, 2013.10.1016/j.yofte.2013.07.015

[37] D. Prato, et al. "Event Detection and Localization Using a MIMO Distributed Fiber Sensor with Birefringence and Phase Estimation," in *Proc. of SPIE Optical Sensing and Detection IX*, 2026.10.1117/12.3104760

[38] D. Prato, et. al. "Numerical Model of a Multiple-Input-Multiple-Output Distributed Acoustic Sensor with Joint Phase and Birefringence Estimation," *HAL [Preprint]*, 2026.hal.science/hal-05651524v1

[39] A. Galtarossa, et. al. "Reflectometric Characterization of Hinges in Optical Fiber Links," *IEEE Photon. Technol. Lett.*, vol.20, 2008.10.1109/LPT.2008.921845

[40] T. Feng, et. al. "Distributed polarization analysis with binary polarization rotators for the accurate measurement of distance-resolved birefringence along a single-mode fiber," *Opt. Express*, vol.26, 2018.10.1364/OE.26.025989

[41] L. Costa, et. al. "Localization of seismic waves with submarine fiber optics using polarization-only measurements," *Commun. Eng.*, vol.2, 2023.10.1038/s44172-023-00138-4

[42] M. Wuilpart, et. al., "Measurement of the spatial distribution of birefringence in optical fibers," *IEEE Photon. Technol. Lett.*, vol.13, 2001.10.1109/68.935820

[43] Y. Chen, et. al., "Distributed Fiber Birefringence Measurement Using Pulse-Compression ϕ-OTDR," *Photonic Sens 11*, 2021.10.1007/s13320-020-0604-3

[44] A. Loayssa, "Phase Noise Effects on Phase-Sensitive OTDR Sensors Using Optical Pulse Compression," *J. Lightw. Technol.*, vol.40, 2022. 10.1109/JLT.2021.3138249

[45] D. Chu, "Polyphase codes with good periodic correlation properties (Corresp.)," *IEEE Trans. Inf. Theory*, vol. 18, 1972.10.1109/TIT.1972.1054840.

[46] J. G. Andrews, "A primer on Zadoff Chu sequences," 2022.arXiv:2211.05702.

[47] M. Freire Hermelo and E. Awwad, "Comparative Analysis of Spread-Spectrum Codes for Fibre-Optic Distributed Acoustic Sensing," *[Preprint]*, 2026.Available Online

[48] N. K. Fontaine, et al. "Tunable Long Range OFDR Enabled by Ultrastable SiN ECTL," in *Proc. of ECOC*, 2025.10.1109/ECOC66593.2025.11263385

[49] E. Piñeiro, et al. "Compensation of Phase Noise Impairments in Distributed Acoustic Sensors Based on Optical Pulse Compression Time-Domain Reflectometry," *J. Lightw. Technol.*, vol.41, 2023.10.1109/JLT.2023.3240026

[50] G. Welch and G. Bishop, "An introduction to the Kalman filter," *Tech. Rep.*, TR 95-041, 1995. Available online.